Appl Phys B (2009) 94: 165–173
DOI 10.1007/s00340-008-3261-6

Applied Physics B
Lasers and Optics

Multifunctional Er^{3+}–Yb^{3+} codoped Gd_2O_3 nanocrystalline phosphor synthesized through optimized combustion route

S.K. Singh · K. Kumar · S.B. Rai

Received: 6 July 2008 / Published online: 22 October 2008

Abstract This paper reports the synthesis of high upconversion luminescent Gd_2O_3: Er^{3+}, Yb^{3+} nanophosphor through optimized combustion route using urea as a reducing agent. The paper also reports the first observation of upconversion emission bands extending upto the UV region (335, 366 and 380 nm) in Er^{3+}–Yb^{3+} co-doped phosphor materials. The fuel to oxidizer ratio has been varied to obtain the maximum upconversion luminescence. Three high intensity bands are found at 408, 523–548 and 667 nm due to the $^4G_{11/2} \rightarrow {}^4I_{15/2}$, $^2H_{11/2}$, $^4S_{3/2} \rightarrow {}^4I_{15/2}$ and $^4F_{9/2} \rightarrow {}^4I_{15/2}$ transitions, respectively, along with the other bands. Input excitation power dependence has been studied for different transitions, and the saturation effect and decrease in the slope of different transitions at higher input pump power has been explained. Heat treatments of the samples show change in crystallite phase/size and relative upconversion luminescence intensities of blue, green and red bands. The color of the phosphor emission has shown to be tunable with change in the crystal structure as well as on excitation laser power and Er^{3+}–Yb^{3+} concentration. The property of color tunability of the phosphor material has been used to record the fingerprint in different colors. Also, the future prospect of the nanocrystalline phosphor material as a sensor for temperature, using FIR method, has been explored.

PACS 33.50.Dq · 61.82.Rx · 32.30.Jc

S.K. Singh · K. Kumar · S.B. Rai (✉)
Laser and Spectroscopy Laboratory, Department of Physics, Banaras Hindu University, Varanasi 221005, India
e-mail: sbrai49@yahoo.co.in

1 Introduction

Inorganic luminescent materials (also called phosphors) have been extensively studied for use as the display materials, high definition television (HDTV), plasma display panel (PDP), cathode ray tube (CRT), field emission displays (FED), temperature sensors, latent fingerprint detection and medical diagnostics [1–7]. In recent years, interest in the rare earth doped nanocrystalline host has increased due to their unique optical behavior [8–12]. Luminescent nanophosphors are also attractive in the field of nanobiotechnology as they have dimensions (diameters) in good match with those of biological structures, such as DNA, proteins, and antibodies. They can be used for analytical, diagnostic, and therapeutic purposes [13, 14].

Upconversion (UC) luminescence in these materials mainly originates from the electronic transitions within the 4f shell of the rare earth ions, which is sensitive to the composition and the structure of the host material. It is well established that materials with lower phonon energy are required as the hosts for luminescent ions to minimize nonradiative losses. This is important especially for the upconversion process (UC), because these are very sensitive to quenching by high energy vibrations according to the energy gap law [15]. Gadolinium oxide (Gd_2O_3) seems to be an ideal matrix for preparation of highly luminescent material as it is chemically stable and has low phonon energy (600 cm^{-1} in bulk Gd_2O_3) [16]. The optimization of the luminescence intensity also depends on different other parameters, such as precursor concentration, surface area and crystallite size, morphologies, reactants, and synthesis technique [17–19]. At present, combustion synthesis of phosphors using organic fuels has become attractive because of the advantages (over other conventional methods), e.g., high purity, low processing temperature, homogeneous mixing,

uniform and spherical particle size. Low energy consumption makes this technique most suitable for large scale production.

In the present work, we have synthesized upconversion efficient Er^{3+}–Yb^{3+} codoped Gd_2O_3 phosphor material through optimized combustion route using urea as a reducing agent. Strong UV/Vis upconversion emissions have been observed and possible upconversion mechanisms have been suggested. Input excitation power dependence has been studied for the different transitions and the saturation effect and decrease in the slope at high input pump power has been explained. The effect of urea concentration on the fluorescence intensity and the effect of heat treatment time on the crystallite size, fluorescence intensity and color tunability have been investigated. The effect of varying temperature on the fluorescence intensity has also been studied. The property of color tunability of the phosphor powder has been used to develop the latent fingerprints in different colors. Also, the future prospect of this material as a temperature nanosensor, using Fluorescence intensity ratio (FIR) method, has been explored.

2 Experimental

The solution combustion method was used for the synthesis of the phosphor material. Reagent grade $Gd(NO_3)_3 \cdot 6H_2O$, $Er(NO_3)_3 \cdot 6H_2O$, and $Yb(NO_3)_3 \cdot 6H_2O$ were used, while urea was used as the organic fuel. The composition of the compounds used was

$$(100 - x - y)Gd_2O_3 + xYb_2O_3 + yEr_2O_3,$$

where x was varied from 0.0 to 0.6 mol% and y from 0.0 to 3.5 mol%.

The stochiometric ratios of these compounds were taken and dissolved in a small amount of de-ionized water. Urea was then added to the solution, and the mixture was stirred in a beaker for 2 h to get a homogeneous product with no visible residue. Solution was then heated to 60°C to evaporate the water. As the water content in the solution goes down, the solution changes into a transparent gel. The gel is transferred into a closed furnace maintained at a fixed temperature (∼500°C). Mixture of metal nitrates (oxidizers) and the fuel (urea) undergo spontaneous combustion under heating, and the chemical energy from the exothermic reaction heats the precursor mixture to high temperature. Consequently, large amounts of gases are produced in the reaction together with the flame due to gas-phase reaction of the combustible gases.

Ceramic foam-like product is obtained, which can easily be grinded into a powder of macroscopic particles composed of a very large number of agglomerated nanocrystals. The synthesized samples were heat-treated at different temperatures to form crystallites in the powder. XRD patterns were recorded to confirm the crystallization and the size of the crystallites using 18 kW rotating anode (Cu) based Regaku powder diffractometer fitted with a graphite monochromator in the diffracted beam. The luminescence spectra were recorded by exciting the sample with 976 nm diode laser on a iHR320 (Horiba Jobin Yvon) spectrometer equipped with R928P photon counting PMT. For the fluorescence measurements at different temperatures the sample was prepared in the form of a pellet (12 mm in diameter, 0.5 mm thickness). Small piece of the pellet was placed on a hot plate, and the temperature was also monitored with thermocouples located close to the samples. FTIR spectra of the samples were recorded using Spectrum RX-1 spectrophotometer (Perkin Elmer). Photo-acoustic signals were measured on the home made setup.

3 Results and discussion

3.1 XRD analysis

The prepared phosphor materials were analyzed by XRD to reveal phase compositions and the particle size at different temperatures. The crystallite size was calculated from the XRD pattern following the Scherer equation

$$t = \frac{\lambda \times 0.9}{\beta \times \cos\theta}.$$

Here, t is the crystallite size for the (hkl) plane, λ is the wavelength of the incident X-ray radiation [CuK_α(0.154056 nm)], β is the full width at half maximum (FWHM) in radians, and θ is the diffraction angle for the (hkl) plane. The XRD patterns shown in Fig. 1 are recorded in three conditions: (a) as synthesized, (b) heat-treated at 600°C for 6 hrs, and (c) heat-treated at 900°C for 6 hrs. All the samples were found to be crystalline in nature. In sample (a), the crystalline Gd_2O_3 was found to be present in the single monoclinic phase with the crystallite size lying in the range from 17 to 50 nm. The intense diffraction peaks (corresponding to 2θ) were observed at 26.10, 28.12, 29.32, 30.01, 31.04, 31.56, 32.36, 38.89, 42.27, 47.40, 51.06, 53.84, and 55.63°. These peaks correspond to the (202), (111), (401), (402), (003), (310), ($\bar{1}$12), (600), ($\bar{3}$13), (313), (020), ($\bar{7}$12), and (022) planes, respectively (JCPDS file no 43-1015). After the heat treatment at 600°C for six hours a few extra peaks at $2\theta = 28.6$, 33.18, 56.52 (denoted by *) with low intensity were observed, whose intensity increases with further heat treatment of the sample at higher temperature. The sample goes into a multiphase form with the crystallite size of 16 to 44 nm. These new peaks become quite prominent in the sample which is heat treated at 900°C for six hours. It was observed that these new peaks correspond to (022),

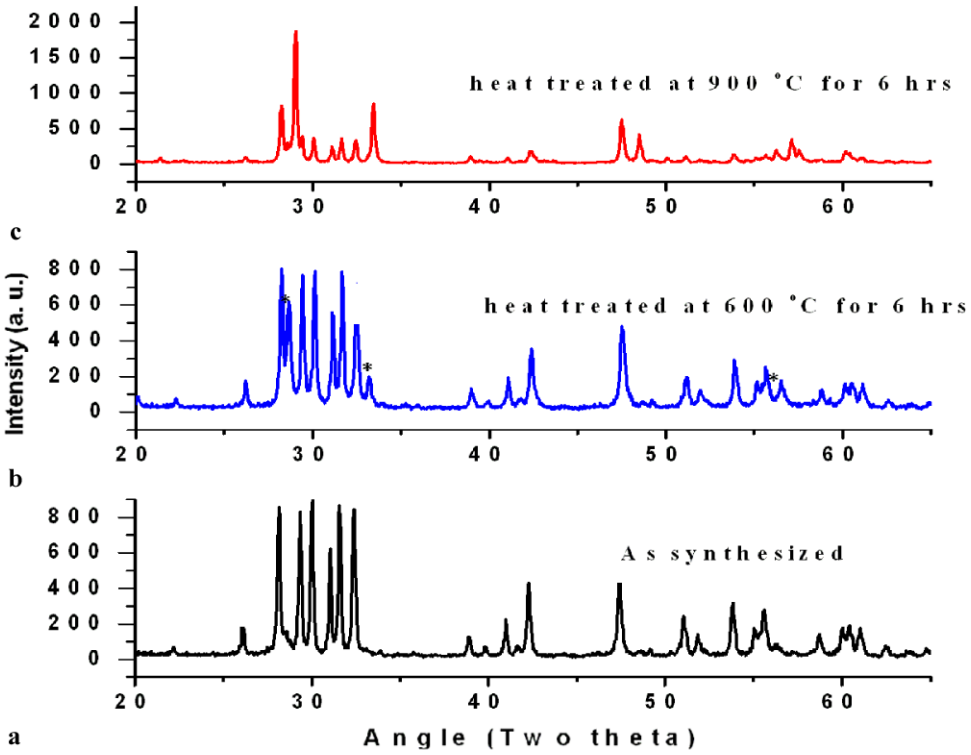

Fig. 1 XRD pattern of Er^{3+}–Yb^{3+} codoped Gd_2O_3 nanocrystals: (**a**) as-synthesized, (**b**) heat-treated at 600°C for 6 hrs, and (**c**) heat-treated at 900°C for 6 hrs

(400) and (622) planes of the cubic crystalline phase of Gd_2O_3 (JCPDS file no 43-1014) with the same crystallite size. Thus, in the sample treated at 900°C for six hours, Gd_2O_3 was found to be in the mixed phase (both monoclinic and cubic phases), and the crystallite size varied in the range of 15–51 nm. Thus, it is observed that as synthesized material is predominantly monoclinic and progressively transformed into the cubic phase by annealing up to 900°C in air, while only a slight variation in crystal size takes place. The same type of observation has also been reported on Gd_2O_3: Eu nanocrystal by Jacobsohn et al. [20].

3.2 The effect of urea concentration

Urea has been used as the reducing agent in the synthesis of the phosphor. Different amounts of urea were used in the synthesis of different phosphor samples to ascertain if urea concentration has any effect on the upconversion property. Previous works on combustion synthesis concluded that it is best to use an initial mixture which is in stoichiometric ratio [21–23]. However, for the present phosphor material, we find that for the best upconversion intensity initial urea content should be much larger than the stoichiometric ratio (Fig. 2). It is found that at lower urea content the temperature obtained during the reduction process is not high enough to remove all traces of the organic residuals which quench the emission intensity. To verify this conjecture, FTIR spectrum of phosphors prepared with (A) low urea content and with (B) high urea content was recorded (see supporting figure). It is seen that in the case of a phosphor prepared with lower urea content, absorption peaks due to the carbonyl and NO_3^- groups (near 1500 and 850 cm^{-1}) and due to the hydroxyl group (near 3400 cm^{-1}) appear with large intensity, while for phosphors synthesized with much higher urea content these peaks become relatively very weak. The decrease in the intensity of the nonradiative transitions was also observed with the help of Photo-acoustic spectroscopy. The sample (A) gives the acoustic signal 160 mV, while the acoustic signal for the sample B (75 mV) at 976 nm wavelength represent a decrease in the nonradiative transition and in the other term an increase in the radiative intensity which supports our above conjecture idea.

3.3 Upconversion emission measurements

The upconversion emission spectra were recorded in the 300–700 nm wavelength region with 976 nm excitation. The emission intensity has been optimized by varying the erbium and ytterbium content in the phosphor, and 0.3 mol% $Er^{3+}$and 2.0 mol% Yb^{3+} led to the best results. Figure 3 shows the emission spectra in the 300–700 nm region for three samples: (a) as synthesized, (b) heat-treated at 600°C for 6 hrs, and (c) heat-treated at 900°C for 6 hrs. The emission is quite intense and is capable to illuminate a 6 m × 4 m room at pump power ∼240 mW. Figure 4 shows photographs of the sample's emission using filters in which emission is seen in three different color regions (blue, green and red) when the input laser power is 240 mW.

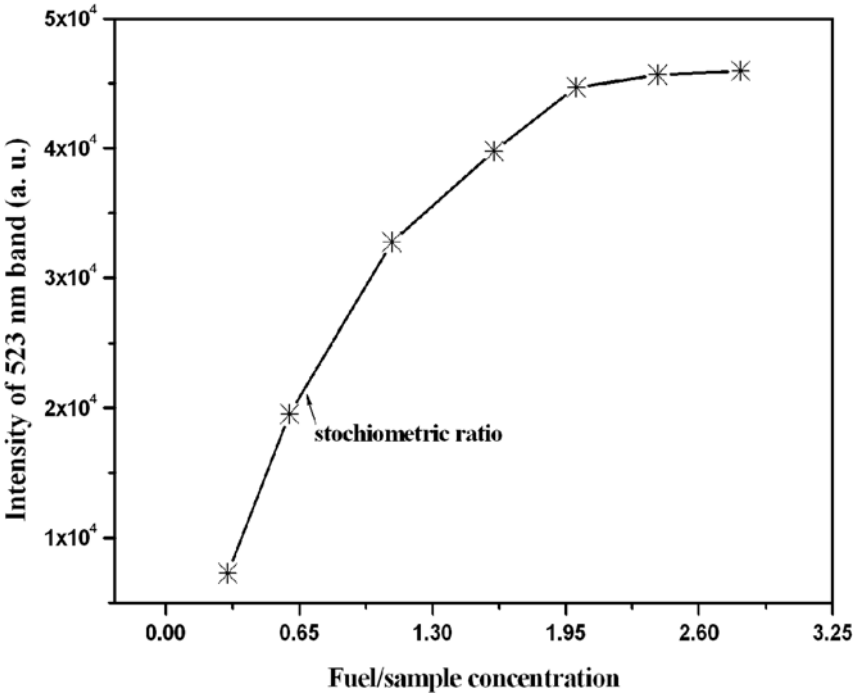

Fig. 2 Variation in the emission intensity of the green ($^4S_{3/2} \rightarrow {}^4I_{15/2}$) band with the concentration of fuel/sample

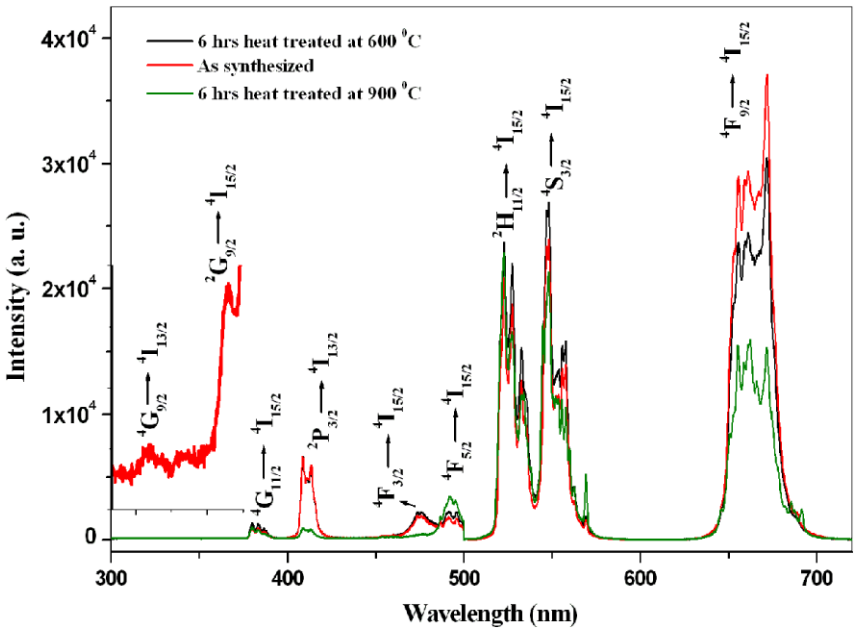

Fig. 3 Upconversion spectra of Er^{3+}–Yb^{3+} codoped Gd_2O_3 nanocrystals for as-synthesized, heat-treated at 600°C for 6 hrs, and heat-treated at 900°C for 6 hrs samples in the region of 300–700 nm

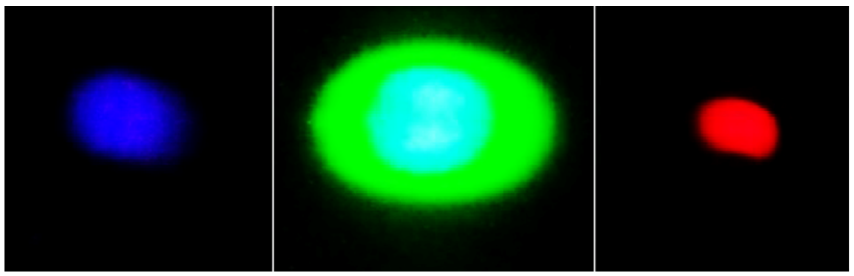

Fig. 4 A photograph of the three colors (*blue*, *green* and *red*) emitted from the as-synthesized sample at the input laser power of 240 mW

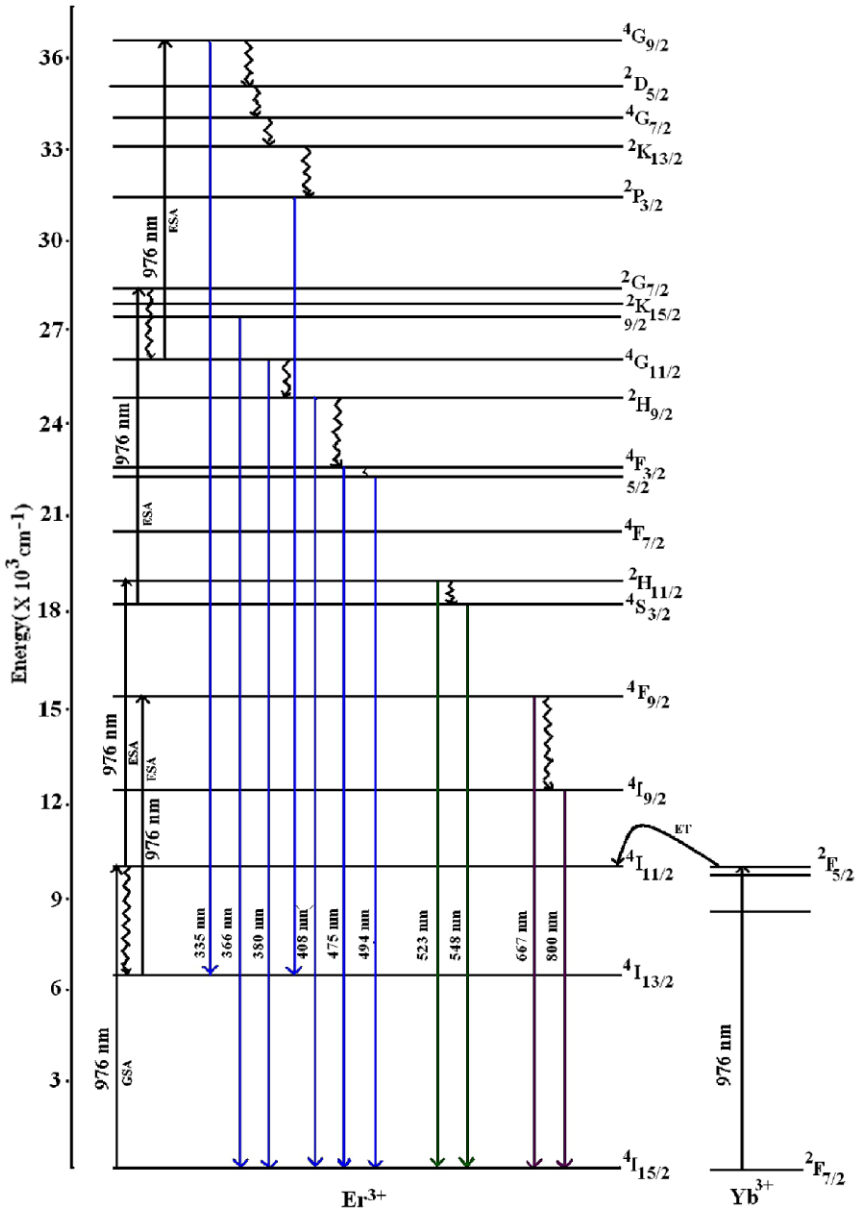

Fig. 5 A schematic energy level diagram of Er^{3+} and Yb^{3+} representing the observed transitions and possible upconversion mechanism

We observe an intense upconversion emissions extending to the UV region in an Er–Yb codoped combustion synthesized phosphor material. Emission is observed at 335, 366, 380, 408, 475, 494, 523, 548, 667, and 800 nm with 976 nm excitation. All these peaks are due to Er^{3+} ion and are ascribed to $^4G_{9/2} \rightarrow {}^4I_{13/2}$, $^2G_{9/2} \rightarrow {}^4I_{15/2}$, $^4G_{11/2} \rightarrow {}^4I_{15/2}$, $^2P_{3/2} \rightarrow {}^4I_{13/2}$ ($^2H_{9/2} \rightarrow {}^4I_{15/2}$), $^4F_{3/2} \rightarrow {}^4I_{15/2}$, $^4F_{5/2} \rightarrow {}^4I_{15/2}$, $^2H_{11/2} \rightarrow {}^4I_{15/2}$, $^4S_{3/2} \rightarrow {}^4I_{15/2}$, $^4F_{9/2} \rightarrow {}^4I_{15/2}$, and $^4I_{9/2} \rightarrow {}^4I_{15/2}$ transitions, respectively. The emission bands show a fairly large Stark splitting due to the large crystal field of Gd_2O_3 matrix. Schematic energy level diagram representing transitions and possible upconversion mechanisms is shown in Fig. 5.

3.3.1 Power dependence and saturation effect

The input power dependence of the emission intensities helps in clarifying the excitation mechanisms and identifies the number of incident photons involved in a particular upconversion transition. Two most common excitation mechanisms involved in upconversion are energy transfer (ET) and excited state absorption (ESA). Figure 6 shows ln–ln plots of the emission intensity (I) versus input pump power (P) for the different emission bands of Er^{3+}. The graph between ln I and ln P normally gives a straight line. The slope of this line is the number of input photons involved in the emission. However, in the present case, the graphs deviate from a straight line at higher pump power. We can discuss it in two parts:

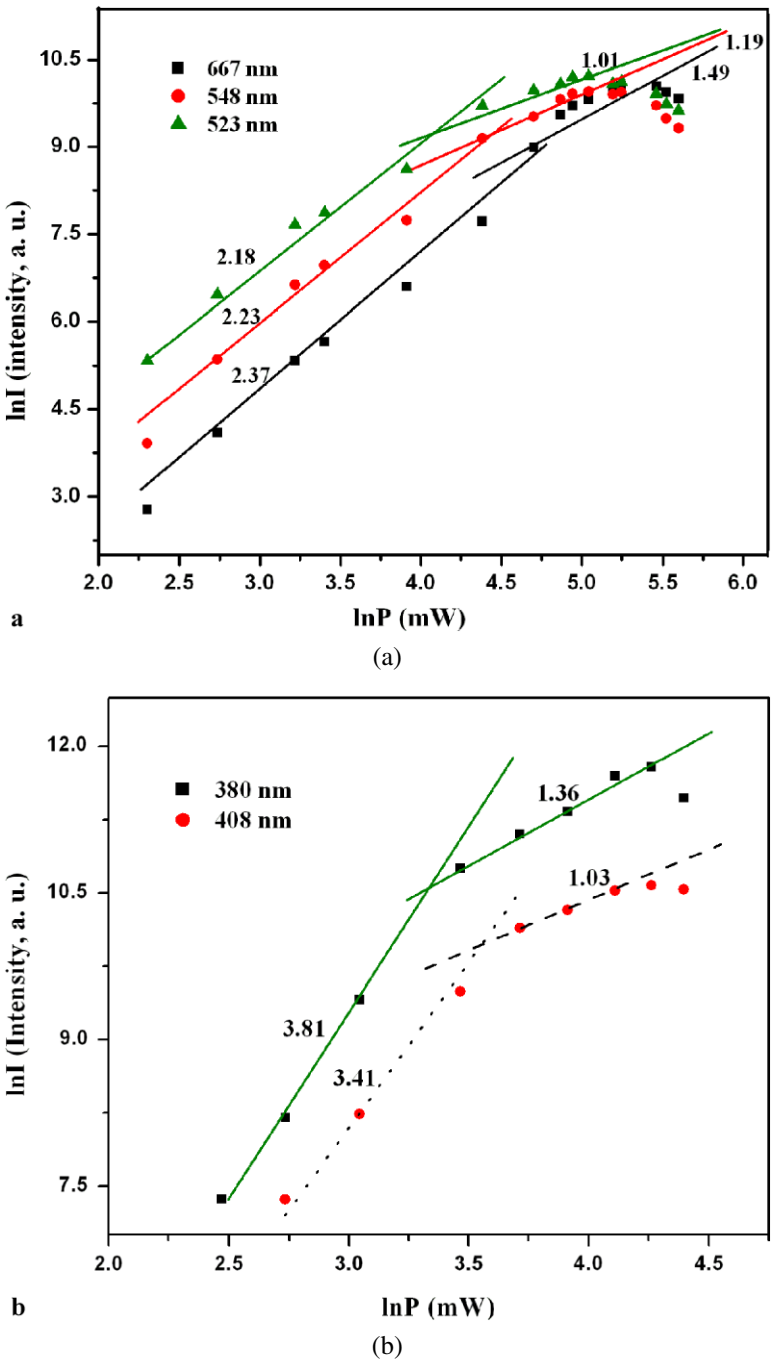

Fig. 6 Power dependence of the upconversion intensity of (**a**) bands at 523, 548 and 667 nm, and (**b**) bands at 380 and 408 nm for the Er^{3+}–Yb^{3+} codoped Gd_2O_3 nanocrystalline phosphor

(A) *Low pump energies*. At low input pump energies the relation $I_{upc}\ \alpha\ (I_{exc})^n$ seems to hold well with $n \sim 2$ or 3. From Fig. 6(a), the bands at 523, 548 and 667 nm yield $n = 2.18$, 2.23 and 2.37, respectively, indicating that two incident NIR photons are needed for each emitted photon. Also, the slope was found to be 3.81 and 3.41 for the bands at 380 and 408 nm (Fig. 6(b)), which indicates that four and three input photons, respectively, are involved in these emissions. Involvements of four photons are also supported for 335 and 366 nm bands.

(B) *High pump energies*. From Fig. 6(a) we observe that the three curves corresponding to 523, 548 and 667 nm emissions approach one another and get superposed on one another for high pump energy. It appears that initially the population of these levels increases with the increase of pump power and the fluorescence from these levels reflects this. As the pump power is increased, saturation takes place and thermal equilibrium is set up in between different levels. This leads to a decrease in the intensity of all these emissions. The slope of the curves is reduced to 1.01, 1.19 and

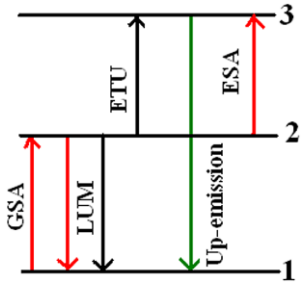

Fig. 7 A simple three level system to understand the decrease in slope values with increasing pump power

1.49, respectively. Similarly, in the case of emission at 380 and 408 nm (Fig. 6(b)), the slope is 1.03 and 1.36, respectively. Similar behavior of ln I –ln P curve has also been reported in Ho^{3+}–Yb^{3+} in $YAlO_3$ crystal by Osiac et al. [24].

The decrease in the value of n (or the slope of the ln I–ln P curve) at increased pump power can be understood by considering a three level system as shown in Fig. 7. Assuming that the pump photon is absorbed by the rare earth ion in its ground state (GSA) with subsequent upconversion either through ETU or through ESA (excluding other terms effecting the population of the upper levels, such as pumping through sensitizer, ground state bleaching, etc.), the rate equations can be written as:

$$dN_2/dt = \rho_p \sigma_1 N_1 - 2W_2 N_2^2 - A_2 N_2, \quad (1)$$

$$dN_3/dt = W_2 N_2^2 - A_3 N_3 \quad (2)$$

for ETU, and

$$dN_2/dt = \rho_p \sigma_1 N_1 - \rho_p \sigma_2 N_2 - A_2 N_2, \quad (3)$$

$$dN_3/dt = \rho_p \sigma_2 N_2 - A_3 N_3 \quad (4)$$

for ESA,
where ρ_p is the pump rate, σ_i is the absorption cross section, W_i is the energy transfer constant, and A_i is the spontaneous emission constant. Under steady state excitation, the above equations reduce to

$$\rho_p \sigma_1 N_1 = 2W_2 N_2^2 + A_2 N_2, \quad (5)$$

$$W_2 N_2^2 = A_3 N_3 \rightarrow N_3 \alpha N_2^2. \quad (6)$$

Two cases arise here for both ETU and ESA processes. For the ET process the two cases are

Case (a). If the state 2 decays primarily to the ground state, we can neglect $W_2 N_2^2$ term and (5) gives $N_2 \propto \rho_p \propto P$ (pump power), and thus (6) gives $N_3 \propto N_2^2 \propto P^2$.

Case (b). If the state 2 has a longer decay rate and upconversion is dominant over linear decay, then we can neglect $A_2 N_2$ term in (5) which gives $N_2^2 \propto \rho_p \propto P$, and thus (6) yields $N_3 \propto N_2^2 \propto P$.

Similarly, one can solve for the ESA process under the above two conditions with the results $N_3 \propto P N_2 \propto P^2$ for Case (a) and $N_3 \propto P N_2 \propto P$ for Case (b).

One can thus conclude that increasing pump power increases the upconversion rate, and the slope of the ln I–ln P curve changes from $n \sim 2$ to $n \sim 1$. For an intermediate pumping power regime, a competition between linear decay and upconversion takes place, so the slope lies between the two limiting cases. In practice, ETU and ESA can occur simultaneously with their strength depending on the ion concentration.

The idea is extendable to three and four photons also, and hence changes in the slope from $n \sim 4\&3$ to $n \sim 1$ can be explained in a similar way.

3.3.2 Color tunability

The color tunability of the emission from the synthesized material is another interesting property. The tuning can be achieved either by

1. Choosing proper ratios between Er^{3+} and Yb^{3+} contents,
2. Or by varying incident power density,
3. Or by varying crystal structure.

In the first case, when we increase the content of Yb^{3+} ions in the sample with fixed Er^{3+} ion concentration, the dominant color of the emission band changes from green to red even though the efficiency of the total emission is seen to diminish if the ytterbium content is beyond the critical limit (2.0 mol%). It happens due to the fact that upon increasing the Yb^{3+} concentration, the probability of ET increases and it dominates over ESA (responsible for green emission) process beyond a certain concentration. The most possible ET channel is:

$$^2F_{5/2}(Yb^{3+}) \rightarrow {}^4I_{11/2}(Er^{3+}),$$

$$^4I_{11/2}(Er^{3+}) \rightarrow {}^4I_{13/2}(Er^{3+}) + \text{phonon},$$

$$^4I_{13/2}(Er^{3+}) + h\nu(\text{pump}) \rightarrow {}^4F_{9/2}(Er^{3+}),$$

$$^4F_{9/2}(Er^{3+}) \rightarrow {}^4I_{15/2}(Er^{3+}) + \text{Red phonon}.$$

The pump power differentiates the ESA and ET processes. The ESA process shows a slope value close to 2.0, whereas the ET process deviates from $n = 2.0$ and shows $n \sim 1.5$. Hence, when we excite the sample with low photon density, the ET dominates over ESA but as the photon density increases ET goes behind to ESA. Hence, the color tunability is observed on pump power density.

In the third, the color tunability is observed by change in the crystal structure. From Fig. 3, it is clear that the red emission is stronger in the as-synthesized sample, while after the heat treatment red emission becomes weak and the green emission dominates in intensity. For sample (b), green and red emission intensities are nearly the same, while for sample (c) green emission is stronger than the red one. It is clear from the XRD analysis that the crystallite size is nearly

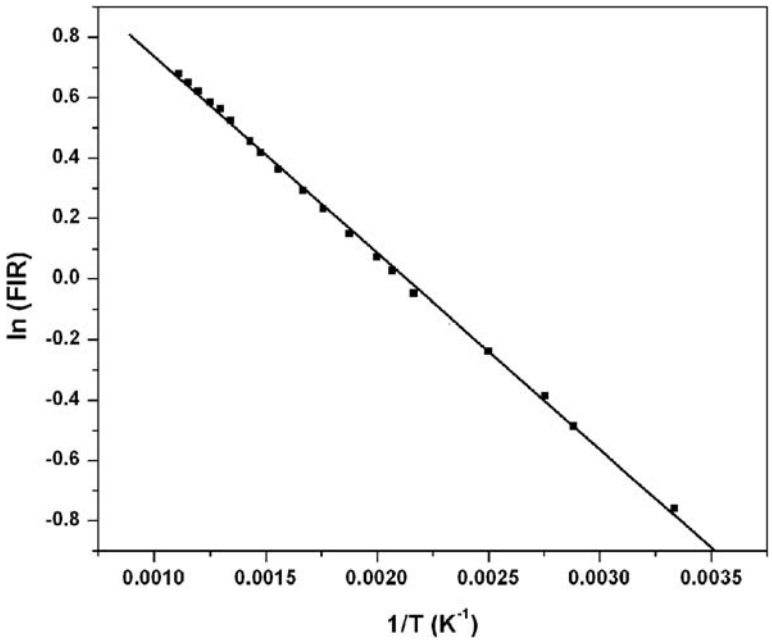

Fig. 8 FIR of the emission bands centered at 523 and 548 nm as a function of inverse absolute temperature on a monolog scale showing a linear dependence

the same in all the three samples. However, sample (a) contains mainly the monoclinic phase of Gd_2O_3, while in the case of sample (b) the cubic phase is also present though less prominent, and finally in the sample (c) the cubic phase becomes the prominent one. The color of the emission thus seems to be directly related to the crystal structure.

3.4 Temperature dependence (Temperature sensor)

The effect of temperature on the upconversion intensities of the transitions has also been studied in detail. It is found that overall fluorescence intensity decreases with an increase in temperature. The $^2H_{11/2}$ and $^4S_{3/2}$ levels of Er^{3+} are quite close to each other and are thermally coupled to each other. Fluorescence intensity ratio (FIR) of the fluorescence arising from the levels $^2H_{11/2}$ and $^4S_{3/2}$ to ground state of Er^{3+} has been measured in the temperature range of 300–900 K. Figure 8 shows the variation of the FIR for the emission bands centered at 523 and 548 nm as a function of inverse absolute temperature on a monolog scale which yields a linear dependence.

The use of this material as a possible temperature sensor has two advantages: first, the operating temperature range ~1200°C which is much higher compared to the glasses, such as fluoroindate, chalchogenide, fluoride, and tellurite (200–300°C) [25]. Silica host also allows a relatively wide temperature range (640°C), but the main drawback of this host is its relatively low fluorescence efficiency [26]. Second, due to nanocrystalline structures of the present phosphor, temperature sensitivity could also be improved because the nanocrystals permit greater intensity ratio variation with temperature [27].

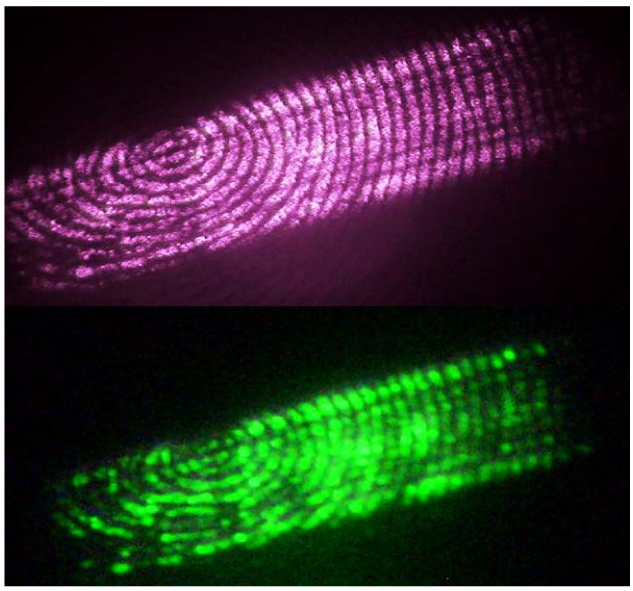

Fig. 9 A fingerprint developed in two different colors (*red* and *green*) using Er^{3+}–Yb^{3+} codoped Gd_2O_3 nanocrystalline powder illuminated by a 976 nm diode laser

3.5 Fingerprint detection using Er^{3+}–Yb^{3+} codoped Gd_2O_3 nanocrystalline powder

Fingerprints were developed by using the as-synthesized sample on three different surfaces: (i) glass plate, (ii) metal surface, and (iii) fresh leaf. The phosphor nanopowder was sprinkled on the finger marks on the three surfaces using conventional powder dusting technique [4] and then illuminated by a 976 nm diode laser. All the images were monitored simply by a Kodak Easyshare CX6330, 3.1 megapixel

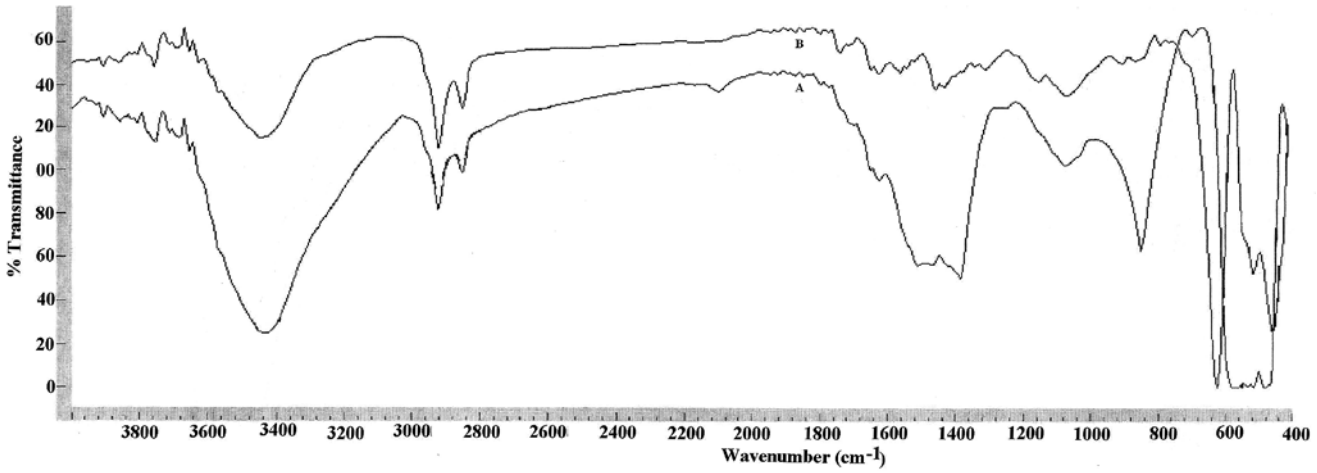

Supporting Fig. 1 FTIR spectra of (**A**) urea concentration taken in stoichiometric ratio, (**B**) at high urea concentration

camera. Fingerprints developed in two different colors (red and green) on the glass plate with the help of the variation in laser power are shown in Fig. 9. It is evident from the figure that the luminescence of the Er^{3+}–Yb^{3+} codoped Gd_2O_3 nanocrystalline powder provides a good contrast between the fingerprint ridges and the background. Much better finger marks can be observed using still better imaging devices. Since emission color varies with different parameters, this powder would also be quite useful for fingerprinting from colored surfaces.

4 Conclusions

Er^{3+}–Yb^{3+} codoped Gd_2O_3 nanocrystalline phosphor material has been synthesized through optimized combustion route. Material gives strong upconversion emissions in UV, blue, green, and red regions. Change in the color of the emission and the intensity was observed and attributed to the monoclinic to cubic structural transformation in the Gd_2O_3 nanocrystallite arising due to the thermal treatment of the sample. The phosphor nanopowder has been found suitable for latent fingerprint development in different colors as well as for a temperature nanosensor.

Acknowledgements Authors are grateful to Forensic Science Department (DFS, MHA, New Delhi) and CSIR, New Delhi for financial assistance.

References

1. G. Blasse, B.C. Grabmaier, *Luminescent Materials* (Springer, Berlin, 1994)
2. C. Feldmann, T. Jusatel, C.R. Ronda, P.J. Schmidt, Adv. Funct. Mater. **13**, 511 (2003)
3. M. Zhang, J. Wang, W. Ding, Q. Zhang, Q. Su, Appl. Phys. B **86**, 647 (2007)
4. C. Champod, C. Lennard, P. Margot, M. Stoilovic, *Fingerprint and other ridge skin impression* (CRC Press, Boca Raton, 2004)
5. P.C. Brownrigg, S.A. Pollack, V. Vali, U.S. Patent number-5099131, 1992
6. V.K. Rai, Appl. Phys. B **88**, 297 (2007)
7. M. Pollnau, D.R. Gamelin, S.R. Luthi, H.U. Gudel, Phys. Rev. B **61**, 3337 (2000)
8. N.G. Subramaniam, S.S. Pandian, T.W. Kang, Appl. Phys. B **80**, 935 (2005)
9. K. Riwotzki, H. Meyssamy, H. Schnablegger, A. Kornowski, M. Haase, Angew. Chem. **113**, 574 (2001)
10. G.A. Hebbink, J.W. Stouwdam, D.N. Reinhoudt, F.C.J.M. van Veggel, Adv. Mater. **14**, 1147 (2002)
11. X. Wang, Y.D. Li, Angew. Chem. **114**, 4984 (2002)
12. X. Wang, X.M. Sun, D.P. Yu, B.S. Zhou, Y.D. Li, Adv. Mater. **15**, 1442 (2003)
13. P.L.A.M. Corstjens, M. Zuiderwijk, M. Nilsson, H. Feindt, R.S. Niedbala, H.J. Tanke, Anal. Biochem. **312**, 191 (2003)
14. O.V. Salata, J. Nanobiotec. **2**, 3 (2004)
15. S.I. Klink, G.A. Hebbink, L. Grave, F.C.J.M. van Veggel, D.N.R. Reinhoudt, L.H. Slooff, A. Polman, J.W. Hofstraat, J. Appl. Phys. **86**, 1181 (1999)
16. Y. Lie, H. Song, L. Yang, L. Yu, Z. Liu, G. Pan, X. Bai, L. Fan, J. Chem. Phys. **123**, 174710 (2005)
17. W.N. Wang, W. Widiyastuti, T. Ogi, I.W. Lenggoro, K. Okuyama, Chem. Mater. **19**, 1723 (2007)
18. K.Y. Jung, C.H. Lee, Y.C. Kang, Mater. Lett. **59**, 2451 (2005)
19. L.S. Wang, Y.H. Zhou, Z.W. Quan, J. Lin, Mater. Lett. **59**, 1130 (2005)
20. L.G. Jacobsohn, B.L. Bennett, R.E. Muenchausen, S.C. Tornga, J.D. Thompson, O. Ugurlu, D.W. Cooke, A.L. Lima Sharma, J. Appl. Phys. **103**, 104303 (2008)
21. H. Li, X. Liu, L. Huang, Ceram. Intern. **33**, 1141 (2007)
22. S.R. Jain, K.C. Adiga, P.V. Verneker, Combust. Flame **40**, 71 (1981)
23. H. Ryul, K.S. Bartwal, Res. Lett. Mater. Sci. **23**, 23643 (2007)
24. E. Osiac, I. Sokolska, S. Kuck, J. Lumin. **95**, 289 (2001)
25. K.M. Lin, Y.Y. Li, Nanotechnologies **17**, 4048 (2006)
26. S.A. Wade, S.F. Collins, G.W. Baxter, J. Appl. Phys. **94**, 4743 (2003)
27. M.A.R.C. Alencar, G.S. Maciel, C.B. de Araujo, Appl. Phys. Lett. **84**, 4753 (2004)